The University of Sydney
Department of Civil Engineering
Sydney NSW 2006
AUSTRALIA

http://www.civil.usyd.edu.au/

Centre for Advanced Structural Engineering

Numerical Modelling of Stainless Steel Plates in Compression

Research Report No R813

By

Kim JR Rasmussen MScEng PhD
Tim Burns BE
Paul Bezkorovainy BE
Michael R Bambach BE

March 2002

The University of Sydney

Department of Civil Engineering
Centre for Advanced Structural Engineering
http://www.civil.usyd.edu.au

Numerical Modelling of Stainless Steel Plates in Compression

Research Report No R813

Kim JR Rasmussen MScEng PhD
Tim Burns BE
Paul Bezkorovainy BE
Michael R Bambach BE

March 2002

Abstract:

The report describes the development of numerical models for analysing stainless steel plates in compression. Material tests on coupons cut in the longitudinal, transverse and diagonal directions are included as are the results of tests on stainless steel plates. Detailed comparisons are made between the experimental and numerical ultimate loads, load-displacement curves and load-strain curves. It is shown that excellent agreement with tests can be achieved by using the compressive stress-strain curve pertaining to the longitudinal direction.

The effect of anisotropy is investigated using elastic-perfectly-plastic material models, where the anisotropic material model is based on Hill's theory. The models indicate that the effect of anisotropy is small and that it may not be required to account for anisotropy in the modelling of stainless steel plates in compression.

Keywords:

Plates, stainless steel, finite elements, plasticity, anisotropy, tests.

Copyright Notice

Department of Civil Engineering, Research Report R813
Numerical Modelling of Stainless Steel Plates in Compression

k.rasmussen@civil.usyd.edu.au

Published by:
Department of Civil Engineering
The University of Sydney
Sydney, NSW, 2006
AUSTRALIA

March 2002

http://www.civil.usyd.edu.au

1 Introduction

Stainless steel alloys are found in a wide range of structural applications, including two and three dimensional truss structures, canopy structures and other roof structures featuring the aesthetic appeal of the material, including roof sheeting. The thickness is often kept at a minimum to reduce the relatively high material cost and achieve solutions with high strength to weight ratios. Many structural applications are cold-formed and may suffer from local or distortional buckling in their ultimate limit state.

Despite the prevalence of local buckling in the design of stainless steel structural members, little research data exists and the available research (Johnson and Winter 1966, van den Berg 2000, SCI 2000) is primarily experimental. The present report forms part of an ongoing investigation into the strength of stainless steel plate elements. It describes the development of finite element models which incorporate the material characteristics of stainless steel alloys. The models are shown to produce good agreement with tests on stainless steel plates. They are currently being used to produce data for the design of stainless steel plates in compression, as will be described in a companion report.

Stainless steel alloys are characterized by having different properties in compression and tension and different properties in the transverse and longitudinal directions, as illustrated in Fig. 1 for annealed austenitic AISI304 alloy. These characteristics require careful material modelling particularly in the case of plated structures in compression which develop two-dimensional stress states during buckling. Furthermore, in contrast to structural steels, which have a yield plateau and may be modelled as elastic-perfectly-plastic, stainless steel alloys have nonlinear stress-strain curves featuring low proportionality stress, no yield plateau and extensive strain-hardening capability, as also shown in Fig. 1.

In numerical analyses, the modelling of nonlinear stress-strain curves is straightforward in most finite element packages, including Abaqus which has been used for the present study. However, these material models assume *isotropic* nonlinear hardening and as such cannot model stainless steel alloys accurately. Abaqus includes a facility for modelling anisotropy based on Hill's theory (Hill 1950) which has been used in the present report to study the effect of anisotropy on the buckling of plates. However, the anisotropic theory assumes the material is *elastic-perfectly-plastic* and cannot account for strain hardening.

The purpose of this report is to present test results and the development of finite element models for stainless steel plates. Recent tests on simply supported plates in uniform compression are described and detailed comparisons are made between the experimentally and numerically obtained load-displacements and load-strain curves. To obtain data for the anisotropic material model, results are included for compression and tension tests on coupons cut in the longitudinal, diagonal and transverse directions.

2 Tests

2.1. Plate tests

Two tests were conducted on single plates cut from nominally 3 mm thick UNS31803 stainless steel plate, popularly known as Duplex 2205. The nominal widths were chosen as 125 mm and 250 mm, which corresponded to plate slenderness values ($\lambda=\sqrt{\sigma_y/\sigma_{cr}}$) of 1.03 and 2.06 respectively when using nominal values of yield stress and initial Young's modulus of 440 MPa and 200,000 MPa respectively. The nominal length of the plates was 750 mm which produced aspect ratios of 6 and 3 for the 125 mm and 250 mm wide plates respectively. The plates were guillotined to size. They were simply supported along all four edges in the test rig.

The measured value of thickness was 3.02 mm. The widths were measured as 126.0 mm and 250.7 mm for the nominally 125 mm and 250 mm wide plates respectively. The measured material properties are detailed in the section following. The 125 mm and 250 mm wide test specimens have been referred to as SS125 and SS250 respectively.

Figure 2 shows a photograph of test specimen SS250. The plate test rig used the "finger principle" developed at Cambridge University to a) provide simple supports at the longitudinal supports and b) ensure that the axial thrust was not transferred to the longitudinal supports. The fingers supported the plates at a distance of 4 mm from the longitudinal edges. Bearings were used at the loaded ends to allow flexural rotations. The plates were subjected to uniform compression and tested under stroke control until failure. Full details of the rig are given in Bambach and Rasmussen (2000).

The instrumentation consisted of strain gauge rosettes attached on both sides of the plates at mid-length, as shown in Fig. 2. Rosettes were attached at the middle and 15 mm from the longitudinal edges, moved in slightly to prevent interference with the finger supports. The rosettes measured the strains in the longitudinal, transverse and diagonal directions. A displacement transducer frame was placed over the rig to measure the deflection along the centre of the plate (not visible in Fig. 2). A transducer was mounted on a plate sliding along linear bearings so that by taking frequent readings the longitudinal profile of the plate deflection could be obtained. The deflections were also measured prior to the test to obtain the initial out-of-flatness.

The ultimate loads of test specimens SS125 and SS250 were 155.6 kN and 170.2 kN respectively. Specimen SS125 failed by inelastic buckling with negligible deflections developing until after the ultimate load. Specimen SS250 formed three large nearly symmetric buckles prior to reaching the ultimate load.

2.2. Material tests

The material properties of the stainless steel alloy S31803 were obtained from coupon tests of small sample plates cut from the same larger plates as those used for the plate test specimens. Tension and compression coupons were cut from each sample plate in the longitudinal, transverse and diagonal directions so as to obtain data for the anisotropy of the material.

In the tension coupon tests, strain was measured with strain gauges on both sides of the coupon, while extension was measured by an extensometer. A cross-head rate of 0.1 mm/min was used for each tensile coupon test and data was logged at two-second intervals. The tension coupons were tested until fracture.

The nature of compressive behaviour forced the compression coupons to be fairly stocky. Three individual coupons were glued together to form a tri-laminated coupon. The laminations ran in the direction of loading. Each compressive coupon was approximately 9 mm thick and 25 mm wide. The initial length was 62 mm. To prevent buckling in the compressive coupon tests, a purpose-built jig was used, as shown in Figure 3.

The jig restrained the specimen from buckling out-of-plane about its minor axis. The specimen was also not slender enough for major axis buckling to occur. Stain gauges were attached to the central laminate at mid-height. A cross-head rate of 0.1 mm/min was used for each compression coupon and data was logged at two-second intervals as in the tension coupon tests. Each compression coupon test was terminated when the loading plate began to bear upon the compression test jig. This point was easily identified when a marked post-yield increase in stiffness became evident.

The tension coupon dimensions were measured by micrometer prior to testing. An average cross-sectional area was obtained from these dimensions. The compression coupons were assumed to be three times the thickness of an average tension coupon (3.02 mm). This approach ensured that the extra thickness added by the adhesive was not counted in the total cross-sectional area.

Strain gauge readings for each test were averaged to give an average axial engineering strain. The extensometer also provided the elongation after fracture for each tension test. Average axial engineering strain was obtained by dividing the extensometer readings by the initial gauge length of 45 mm. Engineering stress was calculated as the load divided by the initial cross-sectional area. The stress-strain curves obtained from the tension and compression tests are shown in Figs 4a and 4b respectively. Each figure shows three curves corresponding to coupons cut in the longitudinal, transverse and diagonal directions. The full stress-strain curves for longitudinal and transverse tension are shown in Figures A1 and A2 of Appendix A respectively.

The initial elastic modulus was fitted by hand. The initial modulus was then offset by 0.01% and 0.2% plastic strains to obtain the 0.01% and 0.2% proof stresses. The mechanical properties are summarised in Table 1. They include the Ramberg-Osgood parameter (n) calculated as,

$$n = \frac{\ln(20)}{\ln(\sigma_{0.2} / \sigma_{0.01})} \tag{1}$$

where $\sigma_{0.01}$ and are $\sigma_{0.2}$ are the 0.01% and 0.2% proof stresses respectively.

3 Numerical Models

3.1. General

The aim of the numerical modelling was twofold, first to develop accurate finite element (F.E.) models validated against the experimental plate test results. The second aim was to investigate the effects of material anisotropy and the shape of the initial geometric imperfection.

Four F.E. models were made of each of the tested plates, distinguished only by their material modelling and geometric imperfection. The material models were isotropic nonlinearly hardening, isotropic elastic-perfectly-plastic and anisotropic elastic-perfectly-plastic. The geometric imperfection was as-measured or in three half-waves (plate SS250) or six halfwaves (plate SS125) according to the elastic buckling mode. Abaqus version 5.7 (Hibbit et al. 1997) was used for the F.E. analyses.

3.2. Geometric Details

Each of the four models was simply supported on all edges and loaded in uniform compression. The test plates buckled into three (SS250) or six (SS125) half-waves and post-ultimate localisation was observed. Localisation occurs when one of the buckles undergoes considerably more lateral deflection relative to the remaining buckles. To allow this phenomenon to occur in Abaqus the full length of the test plates was modelled. The measured dimensions of the test plates were used. Only half the plates was modelled by utilising symmetry along the longitudinal centreline. This approach was supported by the test observations. Consistent with the test conditions, the longitudinal boundary restraints modelling the longitudinal finger supports were applied along a row of nodes 4 mm from the edge, as shown in Fig. 5.

Figure 5 also shows the model geometry and edge identification. L_EDGE was subject to uniform compression while END was restrained from translation in the direction of loading. END, EDGE and L_EDGE were simply supported. CENTRE was allowed to translate in the X_1 and X_3 directions to allow for Poisson effects and out-of-plane translation respectively. CENTRE was also allowed to rotate about the X_2 axis.

The mesh density was established from a convergence study. 300 elements were used in the X_1 direction while 64 elements were used in the X_2 direction. The 4-node reduced integration shell element 4SR of the Abaqus element library was used for all calculations.

3.3. Imperfection Modelling and Elastic Buckling Analysis

Two imperfection types were used. The first imperfection was six or three identical half-waves for test plates SS125 and SS250 respectively. This corresponded to the first eigenmode for the test plates and was generated from an elastic buckling analysis. The elastic buckling loads for test plates SS125 and SS250 were 169.4 kN and 78.3 kN respectively based on the total width. The maximum amplitudes of each buckle was 0.5 mm and 1 mm for test plates SS125 and SS250 respectively, which were also the geometric imperfections measured at the centre of the plates.

The second imperfection represented the measured imperfection and was in the form of a single slightly asymmetric single half-wave with amplitudes 0.5 mm and 1.0 mm for test plates SS125 and SS250 respectively. The imperfections were generated in a separate load step by applying forces perpendicular to the plate along the centerline. The magnitudes of the forces were adjusted to produce close agreement with the measured imperfections of the test specimens. The deflected shapes obtained from this load step were used as the geometry of the plate in the subsequent nonlinear analysis.

3.4. Material Modelling

Three material models were employed: isotropic strain hardening, isotropic perfect plasticity and anisotropic perfect plasticity. The isotropic nonlinearly hardening material model was based on the average compressive stress-strain curve for the longitudinal direction (LC), as shown in Fig. 4b. Notwithstanding that this material model (Iso-sh-1hw) did not account for anisotropy, it was the most realistic of the three material models.

The stress-strain curve was modelled as a multi-linear curve of true stress against true plastic strain. The conversion from engineering stress and strain into true stress and true plastic strain was obtained by the following formulae:

$$\sigma_t = \sigma_e (1 + \varepsilon_e) \tag{2}$$

$$\varepsilon_{tp} = \ln(1 + \varepsilon_e) - \frac{\sigma_t}{E_o} \tag{3}$$

where the subscripts *t* and *e* refer to "true" and "engineering" respectively, and ε_{tp} is the true plastic strain.

As mentioned in the Introduction, the anisotropic model implemented in Abaqus assumes perfect plasticity. The model (Aniso-pp-1hw) could therefore not represent the actual stress-strain curves but did facilitate a means of assessing the effect of anisotropy on the behaviour and strength of stainless steel plates. To make this comparison, the anisotropic model has been compared with an isotropic elastic-perfectly-plastic model (Iso-pp-1hw) using the same as-measured geometric imperfection. The isotropic elastic-perfectly-plastic model was a bilinear stress-strain curve with elastic modulus taken from the longitudinal compression (LC) coupon test. The yield stress was defined as the 0.2% proof stress obtained from the LC coupon test.

The anisotropic perfect plasticity model defines the yield surface in the form (Hill 1950),

$$f(\boldsymbol{\sigma}) = \left[F(\sigma_{22} - \sigma_{33})^2 + G(\sigma_{33} - \sigma_{11})^2 + H(\sigma_{11} - \sigma_{22})^2 + 2L\tau_{23}^2 + 2M\tau_{13}^2 + 2N\tau_{12}^2\right]^{\frac{1}{2}} \tag{4}$$

where *F*, *G*, *H*, *L*, *M* and *N* are defined as,

$$
\begin{aligned}
F &= \frac{\sigma_0^2}{2}\left(\frac{1}{\sigma_{0,22}^2}+\frac{1}{\sigma_{0,33}^2}-\frac{1}{\sigma_{0,11}^2}\right)=\frac{1}{2}\left(\frac{1}{R_{22}^2}+\frac{1}{R_{33}^2}-\frac{1}{R_{11}^2}\right)\\
G &= \frac{\sigma_0^2}{2}\left(\frac{1}{\sigma_{0,33}^2}+\frac{1}{\sigma_{0,11}^2}-\frac{1}{\sigma_{0,22}^2}\right)=\frac{1}{2}\left(\frac{1}{R_{33}^2}+\frac{1}{R_{11}^2}-\frac{1}{R_{22}^2}\right)\\
H &= \frac{\sigma_0^2}{2}\left(\frac{1}{\sigma_{0,11}^2}+\frac{1}{\sigma_{0,22}^2}-\frac{1}{\sigma_{0,33}^2}\right)=\frac{1}{2}\left(\frac{1}{R_{11}^2}+\frac{1}{R_{22}^2}-\frac{1}{R_{33}^2}\right)\\
L &= \tfrac{3}{2}\left(\frac{\tau_0}{\tau_{0,23}}\right)^2=\tfrac{3}{2}\frac{1}{R_{23}^2}\\
M &= \tfrac{3}{2}\left(\frac{\tau_0}{\tau_{0,13}}\right)^2=\tfrac{3}{2}\frac{1}{R_{13}^2}\\
N &= \tfrac{3}{2}\left(\frac{\tau_0}{\tau_{0,12}}\right)^2=\tfrac{3}{2}\frac{1}{R_{12}^2}
\end{aligned}
\qquad (5)
$$

In Eqn. (5), $\sigma_{0,ii}$ ($\tau_{0,ij}$) is the measured yield stress when σ_{ii} (τ_{ij}) is applied as the only nonzero stress, σ_0 is a reference yield stress, $\tau_0=\sigma_0/\sqrt{3}$ and R_{ij} is the yield stress ratio,

$$R_{11}=\frac{\sigma_{0,11}}{\sigma_0};\quad R_{22}=\frac{\sigma_{0,22}}{\sigma_0};\quad R_{33}=\frac{\sigma_{0,33}}{\sigma_0};\quad R_{12}=\frac{\tau_{0,12}}{\tau_0};\quad R_{13}=\frac{\tau_{0,13}}{\tau_0};\quad R_{23}=\frac{\tau_{0,23}}{\tau_0} \qquad (6)$$

The longitudinal direction (X1) has been nominated as the reference direction in the present study so that σ_0=527 MPa and R_{11}=1. The shear yield stress $\tau_{0,12}$ for the X1-X2 plane has been approximated by $\sigma_{0D}/\sqrt{3}$ where σ_{0D} is the yield stress for the diagonal direction. Furthermore, the yield stress for the through-thickness direction has been assumed equal to σ_0.

The yield stresses have been taken as the 0.2% proof stresses for compression given in Table 1. Hence, the following yield stress ratios were used,

$$R_{11}=1;\quad R_{22}=\frac{617}{527}=1.17;\quad R_{33}=1;\quad R_{12}=\frac{610/\sqrt{3}}{527/\sqrt{3}}=1.16;\quad R_{13}=1;\quad R_{23}=1 \qquad (7)$$

It should be noticed that all six yield stress ratios are required as input in Abaqus even though the stress state is plane so that τ_{13} and τ_{23} are zero and the values of R_{13} and R_{23} are inconsequential.

4 Comparison of F.E. and Experimental Results

4.1. Validation of FE models

4.1.1 Ultimate loads

Tables 2a and 2b compare numerical ultimate loads with test values for plates SS125 and SS250 respectively. For the strain-hardening models Iso-sh-3hw and Iso-sh-1hw, the

numerical ultimate loads were 7.4% and 3.6% less than the test value respectively for plate SS125, and were 0.4% and 1.1% greater than the test value for plate SS250. It follows that for fairly stocky plates with $\lambda \approx 1$, it is necessary to model the actual imperfection to obtain good agreement with test while for more slender plates, which develop appreciable local buckles prior to reaching the ultimate load, the ultimate load is virtually unchanged whether the actual imperfection is modelled or the imperfection is assumed to be in the shape of the elastic buckling mode.

The elastic-perfectly-plastic models Iso-pp-1hw and Aniso-pp-1hw produce significantly higher ultimate loads than the test values, as could be expected. For the more slender plate SS250, the effect of anisotropy is to increase the ultimate load by 0.8% compared to the isotropic model. However, for the stockier plate SS125, the effect of anisotropy is to *decrease* the ultimate load by 0.8% compared to the isotropic model. It is not clear how the ultimate load can decrease by incorporating anisotropic mechanical properties which are higher in the transverse direction than in the longitudinal reference direction. It is possible that different numerical schemes are used in Abaqus for isotropic and anisotropic yielding. In any event, the difference in ultimate load between the isotropic and anisotropic cases is small, suggesting that it may not be required to account for the effect of anisotropy in the modelling of stainless steel plates in compression. However, this conclusion is drawn for elastic-perfectly-plastic material models and may not apply equally to strain hardening models.

4.1.2 Displacement behaviour

The experimental and F.E. load *vs* axial shortening curves for test plates SS125 and SS250 are compared in Figs 6a and 6b respectively. The axial shortening is the decrease in the distance between the loaded ends and the load is the total load on the plate, which is that recorded in the tests and twice that obtained from an F.E. analysis. The Iso_sh_1hw model is generally in close agreement with the test, while the Iso_sh_3hw model is too flexible, particularly for test plate SS125. The elastic-perfectly-plastic models Iso_pp_1hw and Aniso_pp_1hw are nearly coincident demonstrating negligible influence of material anisotropy.

The curves of load *vs* lateral displacement at the centre are compared in Fig. 7 for test plate SS250. The agreement is good for the strain-hardening models up to and slightly beyond the ultimate load when localization occurred. In the test, localization occurred in the central buckle and so the central deflection increased monotonically until the conclusion of the test, as shown in Fig. 7. However, in the F.E. analysis, localization occurred in one of the buckles at the loaded edges and was associated with elastic unloading of the two other buckles. Accordingly the displacement decreased at the centre when localization occurred, as shown in Fig. 7. For test plate SS125, the central deflection was small throughout the test and has not been compared with analytical results.

Figures 8 and 9 of compare the experimental and numerical centre-line profiles for test plates SS125 and SS250 respectively. Figures 8a and 9a are for loads near the local buckling load, Figures 8b and 9b are the deflection profiles at the ultimate load, as obtained in the tests and the numerical analyses (which were not exactly equal), and Figs 8c and 9c are for post-ultimate loads at advanced stages of buckling. There are some

differences in the profiles obtained at the pre-ultimate loads, as shown in Figs 8a and 9a, which suggest that the F.E. models generally overestimate the initial displacements. The profiles obtained from the tests and the Iso-sh-1hw models are in close agreement at the ultimate load, as shown in Figs 8b and 9b, but less so in the post-ultimate range where localization is evident and occurs in different buckles in the test from in the analyses, as shown in Figs 8c and 9c.

4.1.3 Strain behaviour, test plate SS250

Figures 10 and 11 show longitudinal and transverse surface strains respectively for test plate SS250. The strains are recorded at mid-length, 15 mm in from the edge. The numerical curves are obtained from models Iso-sh-1hw and Iso_hw_3hw. The curves shown in Figs 10 and 11 are in good agreement with the measured experimental strains, notwithstanding the generally larger strains obtained from the numerical analysis, which are consistent with the displacement results. The difference between the strains at the top and bottom surfaces is small because of the proximity to the longitudinal supports which prevent flexure.

The difference between the strains at the top and bottom surfaces is significantly more pronounced at the centre of the plate because of plate flexure, as shown in Figs 12 and 13 for the longitudinal and transverse strains respectively. Again the overall agreement is good except near the local buckling load where the numerical analyses exaggerate the strains. The maximum strains are of the order of 5000 με.

Figures B1, B2, B3 and B4 of Appendix B show the curves corresponding to those of Figs 10, 11, 12 and 13 respectively for models Iso_pp_1hw and Aniso_pp_1hw. The difference between the two models is negligible.

4.2. Effect of Initial Imperfection

The ultimate loads predicted by the Iso-sh-3hw and Iso-sh-1hw models differed by 3.8% and 0.7% for test plates SS125 and SS250 respectively, as shown in Table 3. As concluded in Section 4.1.2, it is necessary to model the actual imperfection to obtain close agreement with test for fairly stocky plates with $\lambda \approx 1$, while for more slender plates, which develop appreciable local buckles prior to reaching the ultimate load, the ultimate load is virtually unchanged whether the actual imperfection is modelled or the imperfection is assumed to be in the shape of the elastic buckling mode. However, there is some difference in the load-displacement and load-strain curves of the two models, as shown in Figs 6-13. The difference is most pronounced near the local buckling load where the as-measured single half-wave imperfection delays the development of local buckles and produces better agreement with tests.

4.3. Effect of Material Anisotropy

By examining the load-displacement curves for Abaqus models Iso-pp-1hw and Aniso-pp-1hw as well as the load-strain curves shown in Appendix B, it was concluded that the effect of anisotropy in plates with perfect plasticity is negligible. The difference between ultimate loads predicted by the two models was ±0.8% and the load *vs* displacement and

load *vs* strain curves were nearly coincident, as shown in Figs 6-7 and B1-B4. However, further study into the effects of anisotropy on stainless steel plates with strain hardening could be warranted considering the fact that models Iso-pp-1hw and Aniso-pp-1hw were premised on elastic-perfectly-plastic material modelling.

5 Conclusions

Finite element models have been presented for the analysis of stainless steel plates in compression. It has been shown that excellent agreement with tests can be achieved by using the stress-strain curve for longitudinal compression, assuming isotropic hardening, and modelling the as-measured geometric imperfection (Iso_sh_1hw). The ultimate load obtained using this model was 3.6% less and 1.2% more that the experimental ultimate loads for test plates SS125 and SS250 respectively. Furthermore, the load *vs* axial shortening, load *vs* lateral displacement and load *vs* strain curves closely resemble the experimental curves, particularly for the slender test plate SS250.

The effect of anisotropy has been investigated on the basis of elastic-perfectly-plastic material models. In the anisotropic model, the yield stress for the transverse direction was 17% higher than for the longitudinal direction. The load *vs* displacement curves showed that anisotropy had negligible effect on the load *vs* displacement curves with a maximum difference in ultimate load of 0.8%. However, the effect of anisotropy may be more pronounced in a strain hardening model where anisotropy plays a role at significantly lower stresses than in elastic-perfectly-plastic models.

Comparing the elastic-perfectly-plastic models (Iso-pp-1hw) with the strain hardening models (Iso-sh-1hw) it is evident that it is important to model the nonlinear stress-strain curve in numerical analyses. The ultimate loads obtained using the elastic-perfectly-plastic material model were 8.8% and 5.5% higher than the experimental values for test plates SS125 and SS250 respectively, as shown in Table 2. Furthermore, the displacements are generally underestimated whereas close agreement was obtained using the strain hardening models.

In summary, stainless steel plates can be accurately modelled by using nonlinear strain hardening material models which are based on compression coupon tests for the longitudinal direction. The present study indicates that anisotropy may *not* be important for numerical analyses.

6 References

Bambach, MR and Rasmussen, KJR, “Experimental Techniques for Testing Unstiffened Plates in Compression and Bending”, *Thin-walled Structures, Advances and Developments*, eds J. Zaras, K. Kowal-Michalska and J. Rhodes, Proceedings of the Third International Conference on Thin-walled Structures, Elsevier, pp. 719-727.

Burns, T and Bezkorovainy, P, (2001), *Buckling of Stiffened Stainless Steel Plates*, BE (Honours) Thesis, Department of Civil Engineering, University of Sydney.

Hibbitt, Karlsson and Sorensen, Inc., (1997), "ABAQUS Standard, Users Manual", Vols 1 and 2, Ver. 5.7, USA.

Hill, R, (1950), *The Mathematical Theory of Plasticity*, Ch. XII, Oxford Science Publications, Clarendon Press, Oxford.

Johnson, AL, and Winter, G, (1966), "Behaviour of Stainless Steel Columns and Beams", *Journal of the Structural Division*, American Society of Civil Engineers, Vol. 92, No. ST5, pp. 97-118.

SCI, (2000), "Development of the Use of Stainless Steel in Construction", Main Work Package Reports – Vol. 1, Document RT810, Ver. 01. Work Package 2: Cross-sections – Welded I-sections and Cold-formed Sheeting, *Steel Construction Institute*, London.

Van den Berg, GJ, (2000), "The Effect of Non-linear Stress-strain Behaviour of Stainless Steel on Member Capacity", *Journal of Constructional Steel Research*, Vol. 54, No. 1, pp135-160.

Table 1: Mechanical properties of S31803 alloy from test data

Specimen	E_o (MPa)	$\sigma_{0.01}$ (MPa)	$\sigma_{0.2}$ (MPa)	σ_{ult} (MPa)	n
TT	215250	430	635	831	7.7
LT	200000	310	575	740	4.8
DT	195000	376	565	698	7.4
TC	210000	380	617	-	6.2
LC	181650	275	527	-	4.6
DC	205000	460	610	-	10.6

Table 2a: Numerical models and ultimate loads of test plate SS125

Model	Imperfection Type	Material Type	Ult. Load (kN)	Error* (%)
Iso-sh-3hw	3 symm. Half-waves	Isotropic strain hardening	144.1	-7.4
Iso-sh-1hw	1 asymm. Half-wave	Isotropic strain hardening	150.0	-3.6
Iso-pp-1hw	1 asymm. Half-wave	Isotropic perfect plasticity	169.3	8.8
Aniso-pp-1hw	1 asymm. Half-wave	Anisotropic perfect plasticity	168.0	8.0

* Relative to test value, P_u=155.6 kN

Table 2b: Numerical models and ultimate loads of test plate 250mm

Model	Imperfection Type	Material Type	Ult. Load (kN)	Error* (%)
Iso-sh-3hw	3 symm. Half-waves	Isotropic strain hardening	171.2	0.4
Iso-sh-1hw	1 asymm. Half-wave	Isotropic strain hardening	172.4	1.1
Iso-pp-1hw	1 asymm. Half-wave	Isotropic perfect plasticity	179.9	5.5
Aniso-pp-1hw	1 asymm. Half-wave	Anisotropic perfect plasticity	181.2	6.3

* Relative to test value, P_u=170.5 kN

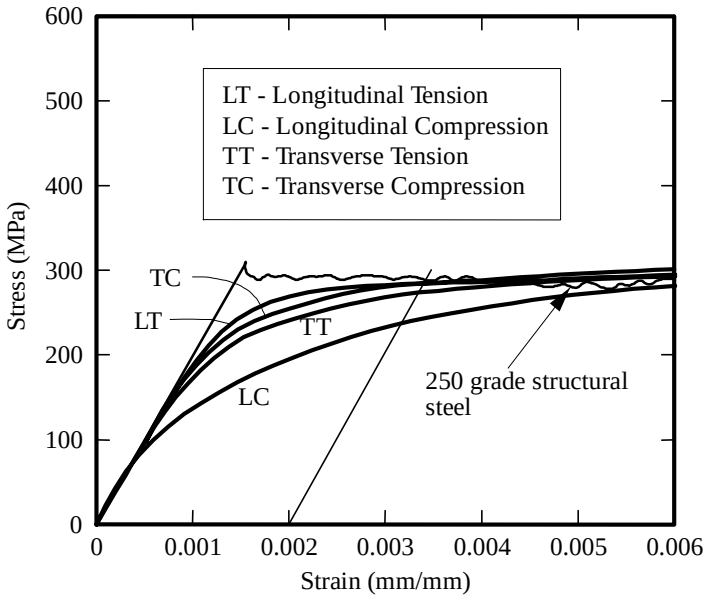

Figure 1. Typical stress-strain curves for austenitic stainless steel alloys and structural steels

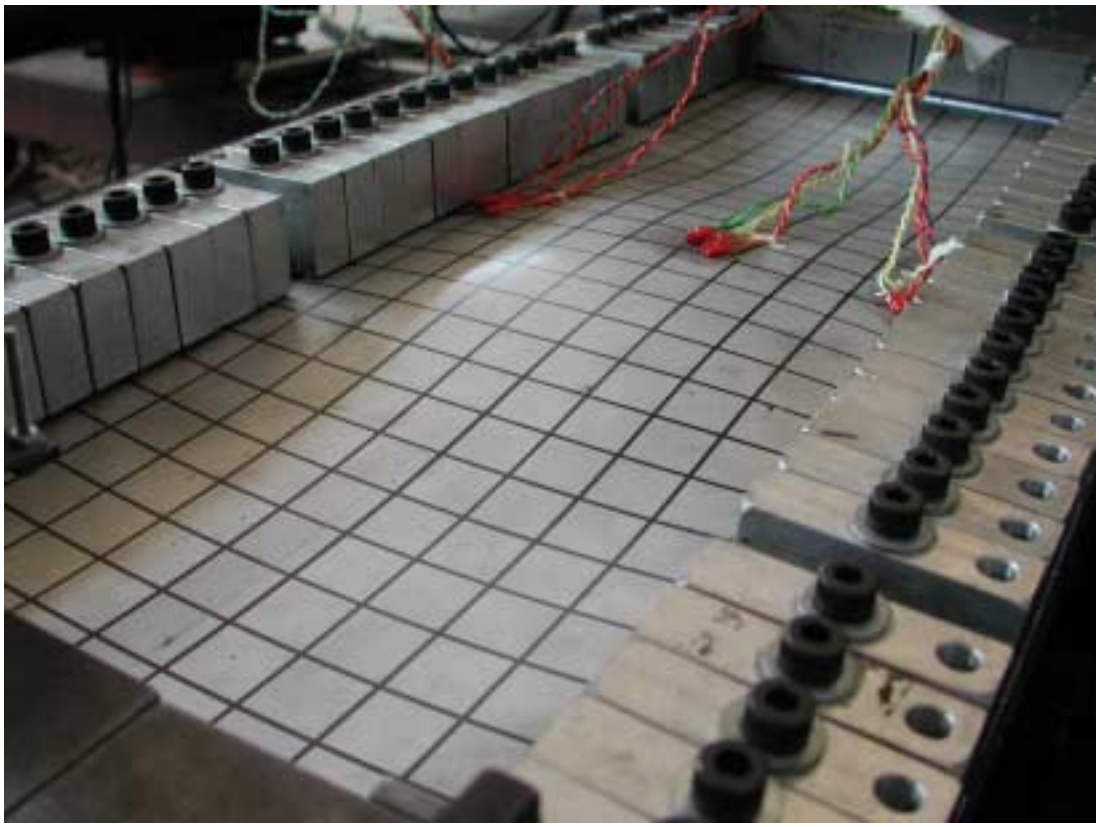

Figure 2: 250mm wide plate during test

Figure 3: Compression test jig

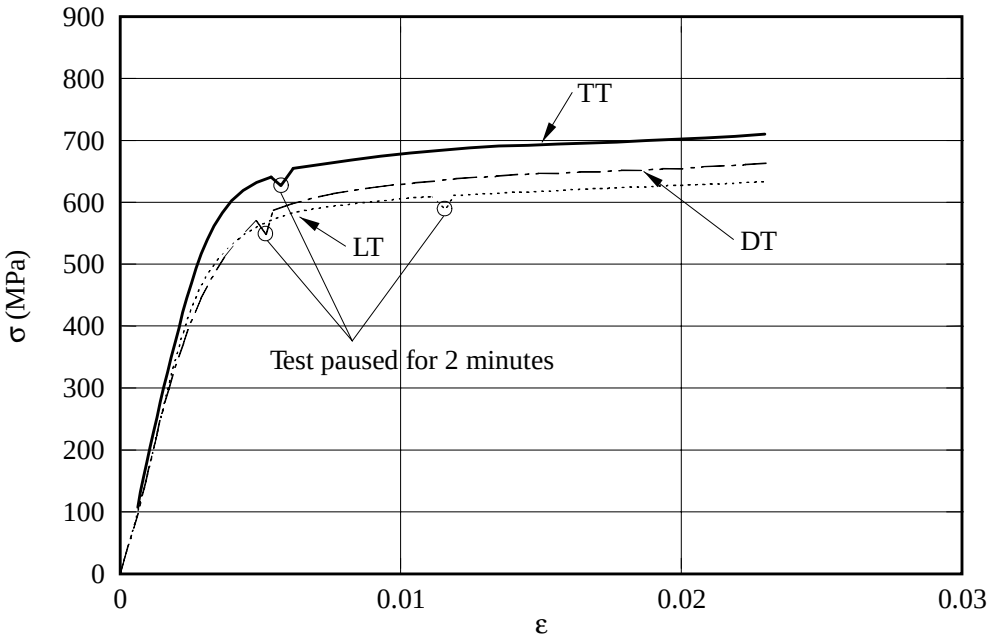

a) Tension; LT~Longitudinal Tension, TT~Transverse Tension, DT~Diagonal Tension

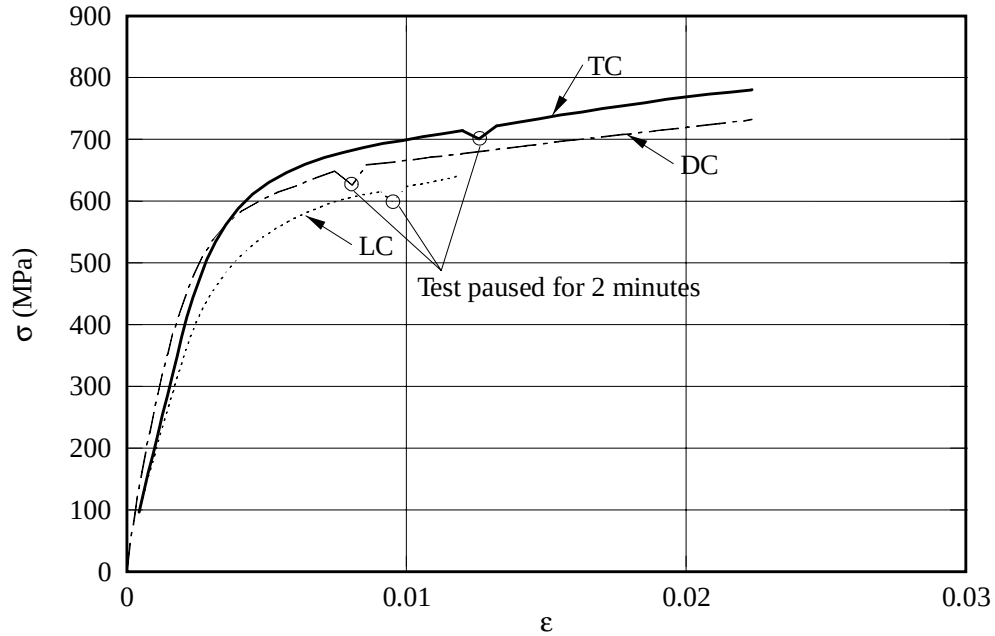

b) Compression; LC~Longitudinal Compression, TC~Transverse Compression, DC~Diagonal Compression

Figure 4: Tension and compression stress-strain curves

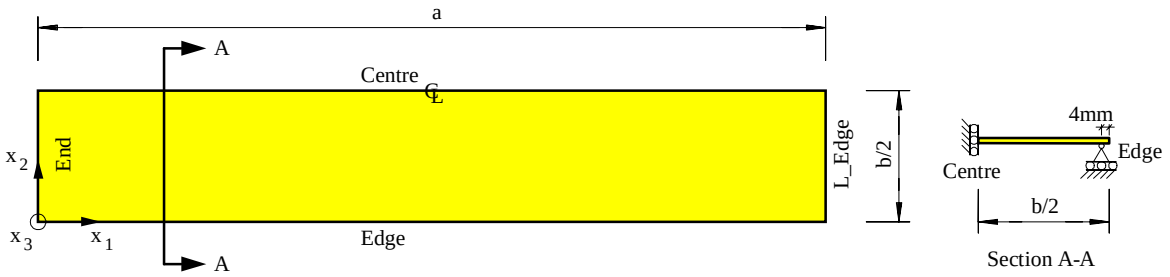

Figure 5: Model geometry

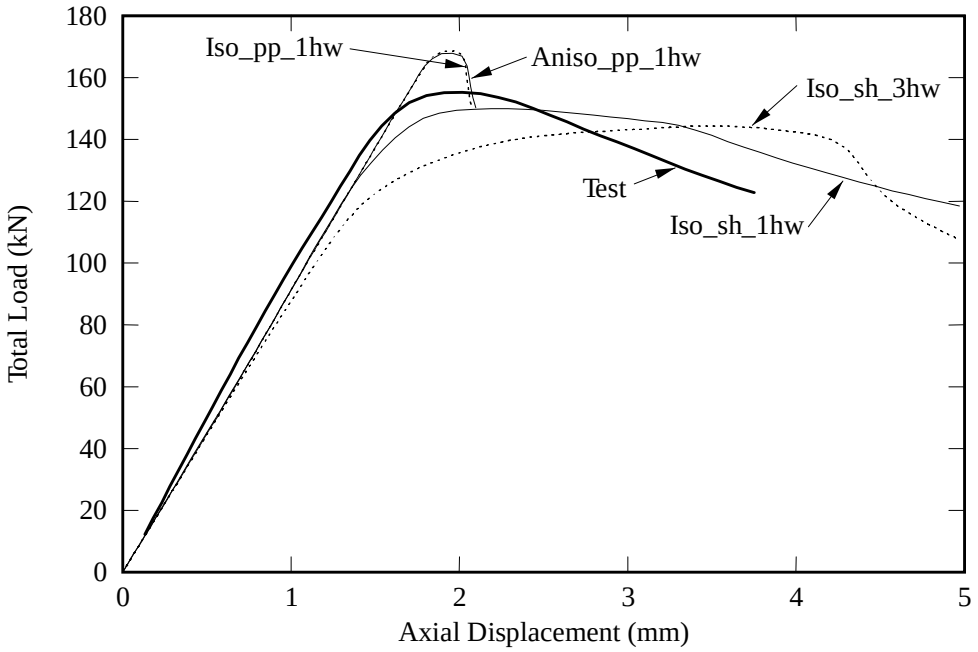

Figure 6a: Load vs Axial Displacement for Plate SS125 and Abaqus Models

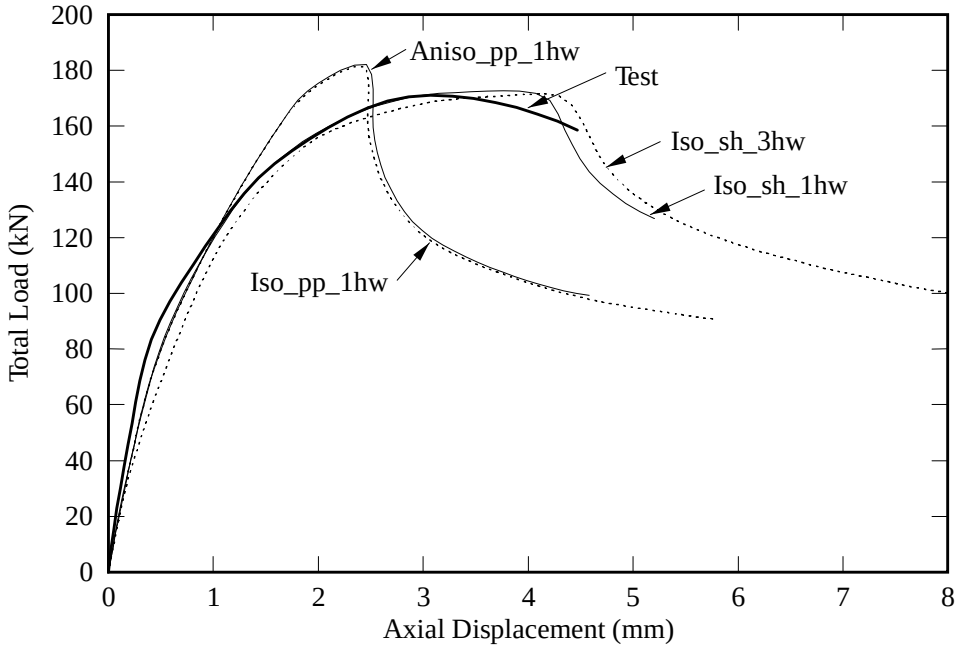

Figure 6b: Load vs Axial Displacement for Plate SS250 and Abaqus Models

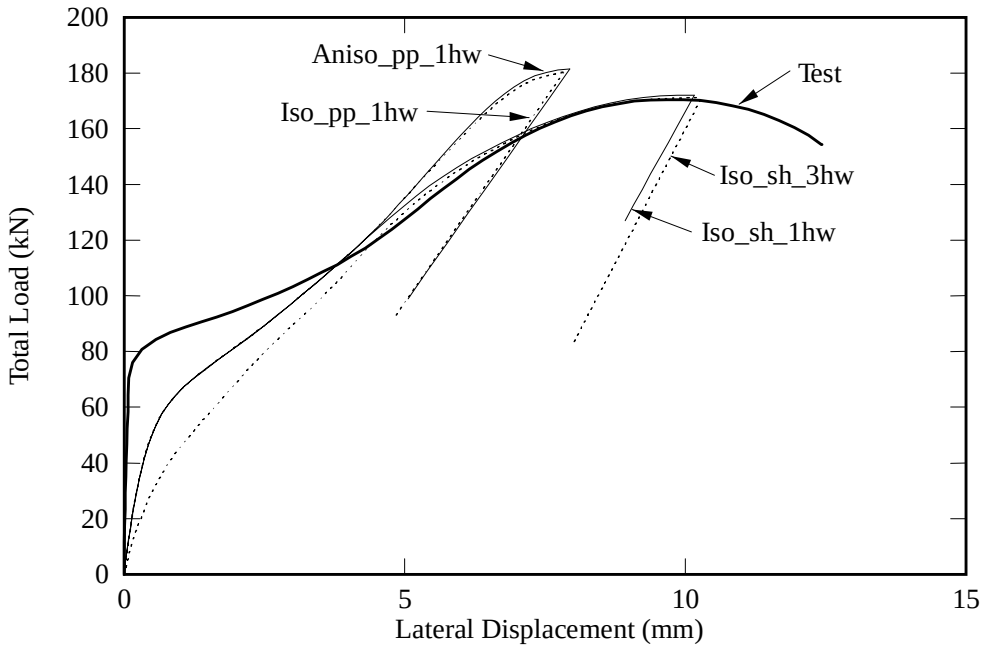

Figure 7: Load vs Lateral Disp. at centre for test plate SS250 and Abaqus Models

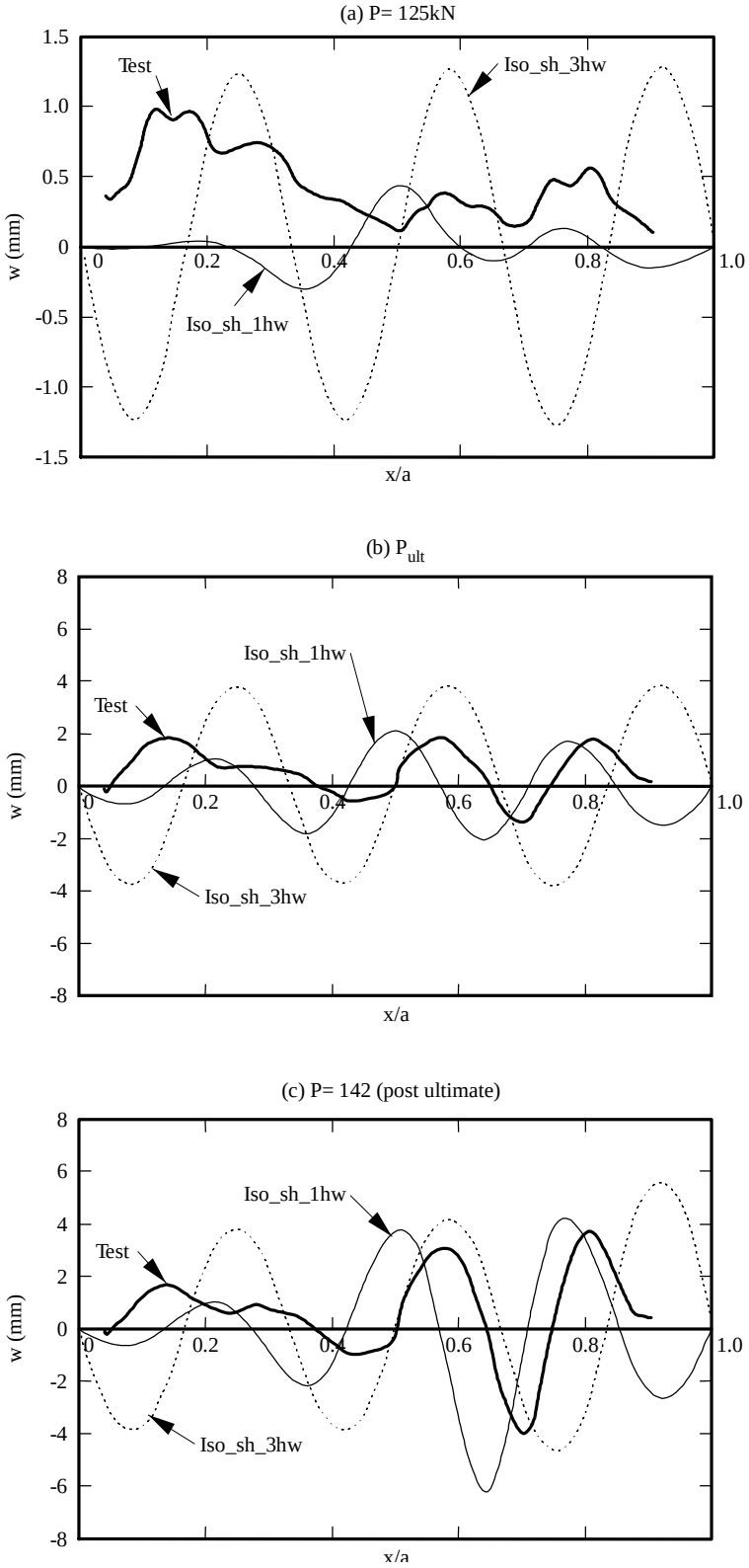

Figure 8: Deflection profiles for Longitudinal Centreline, Test Plate SS125;

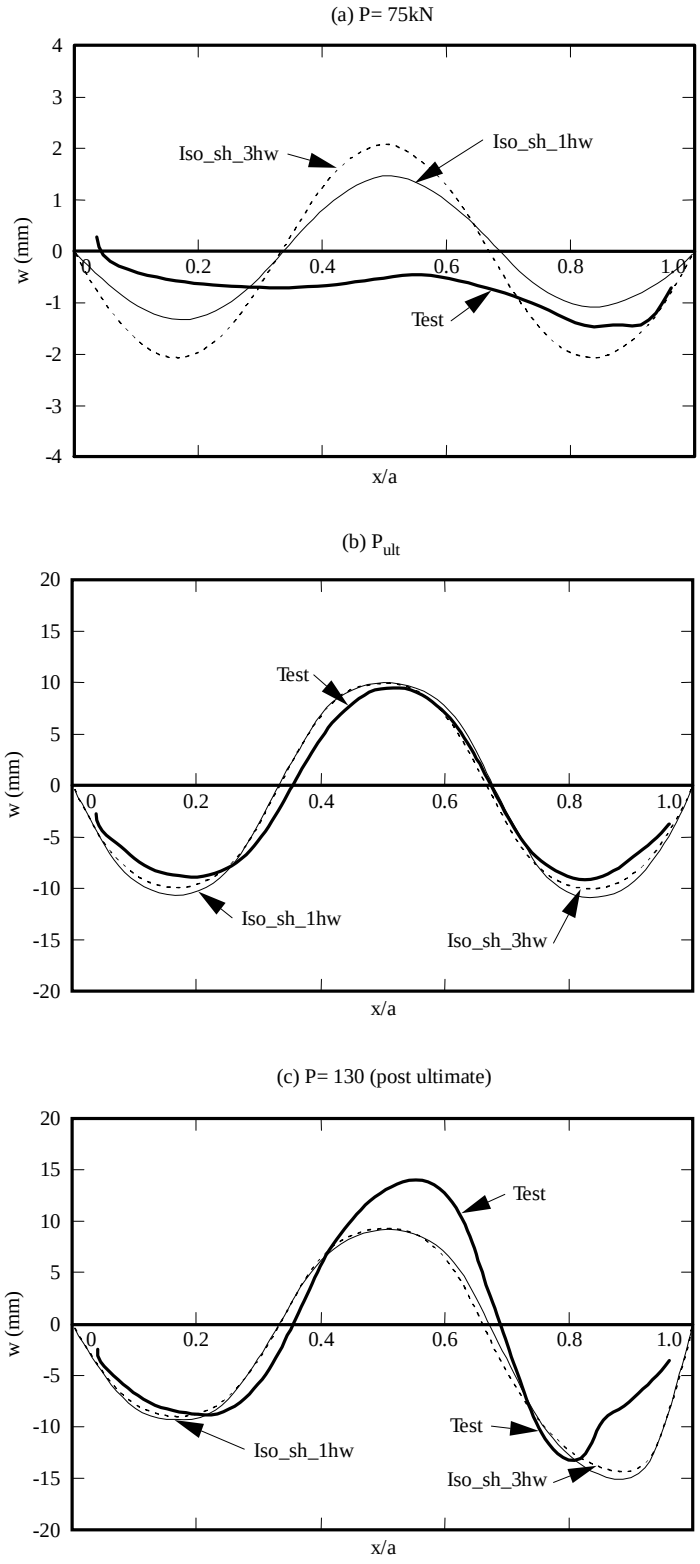

Figure 9: Deflection profiles for Longitudinal Centreline, Test Plate SS250;

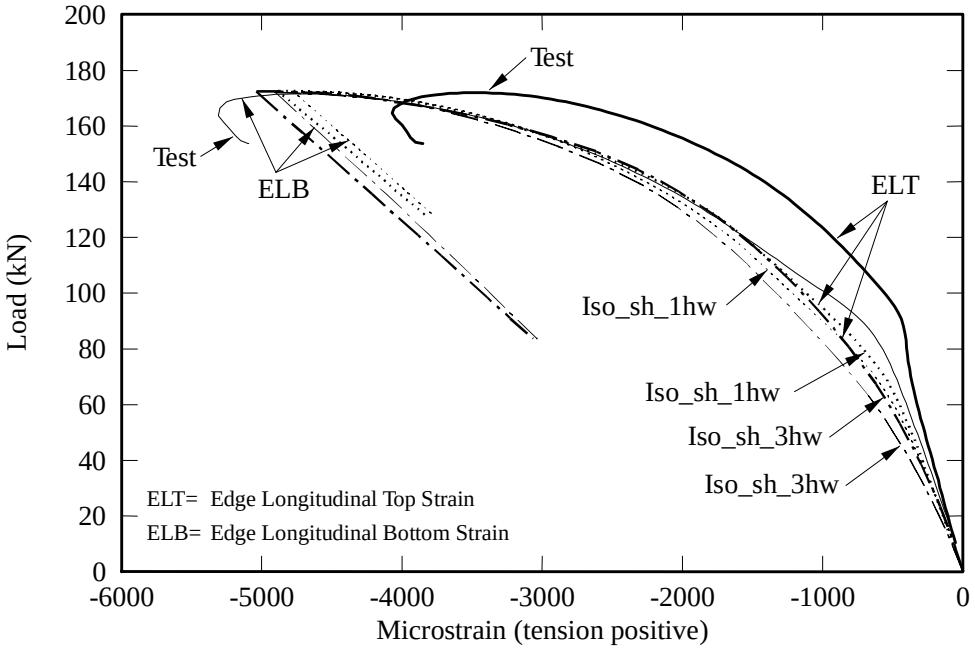

Figure 10: Longitudinal Strains 15 mm from Edge for Test Plate SS250; Test and Abaqus Models Iso-sh-1hw and Iso-sh-3hw

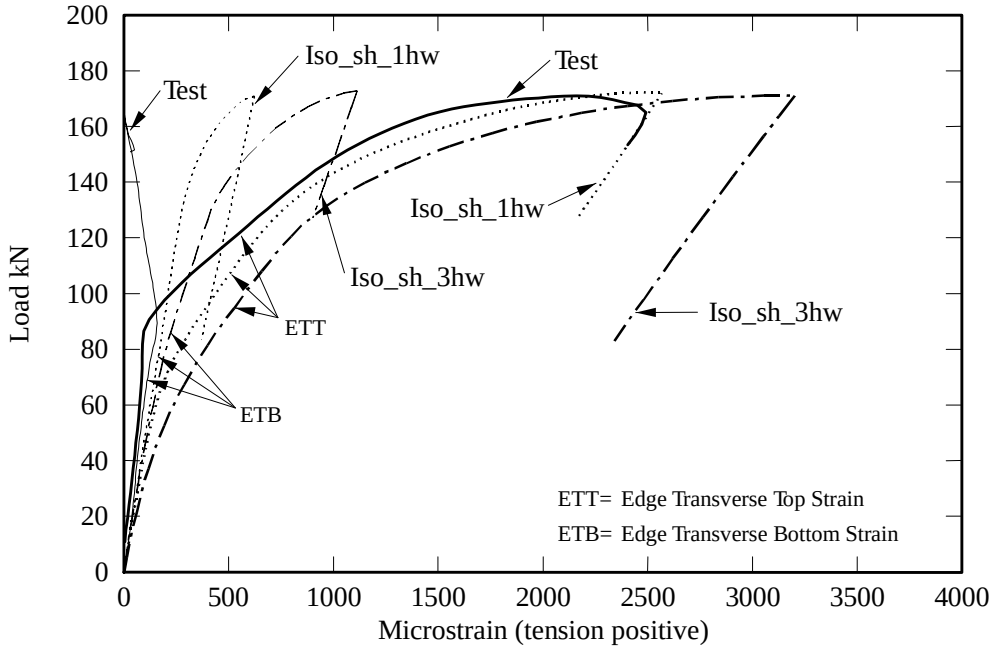

Figure 11: Transverse Strains 15 mm from Edge for Test Plate SS250; Test and Abaqus Models Iso-sh-1hw and Iso-sh-3hw

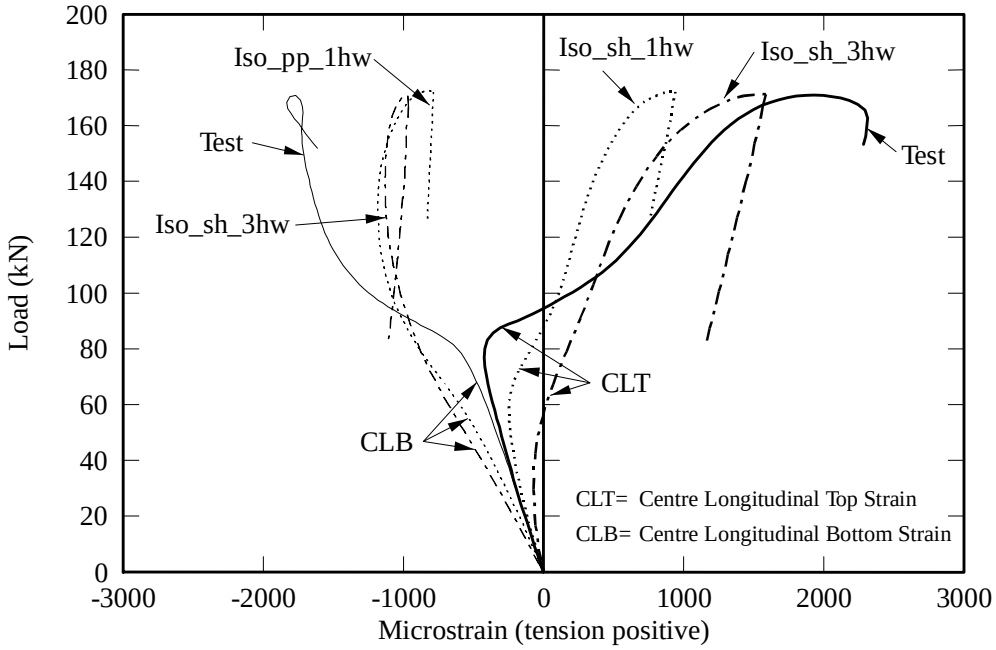

Figure 12: Longitudinal Strains at centre for Test Plate SS250; Test and Abaqus Models Iso-sh-1hw and Iso-sh-3hw

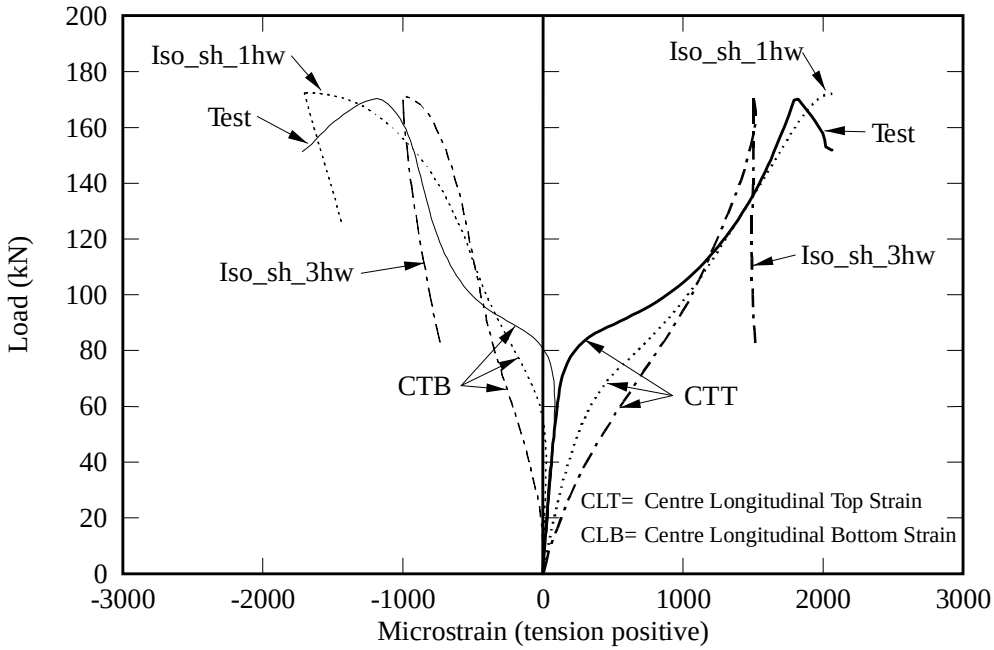

Figure 13: Transverse Strains at centre for Test Plate SS250; Test and Abaqus Models Iso-sh-1hw and Iso-sh-3hw

Appendix A: Stress-strain curves

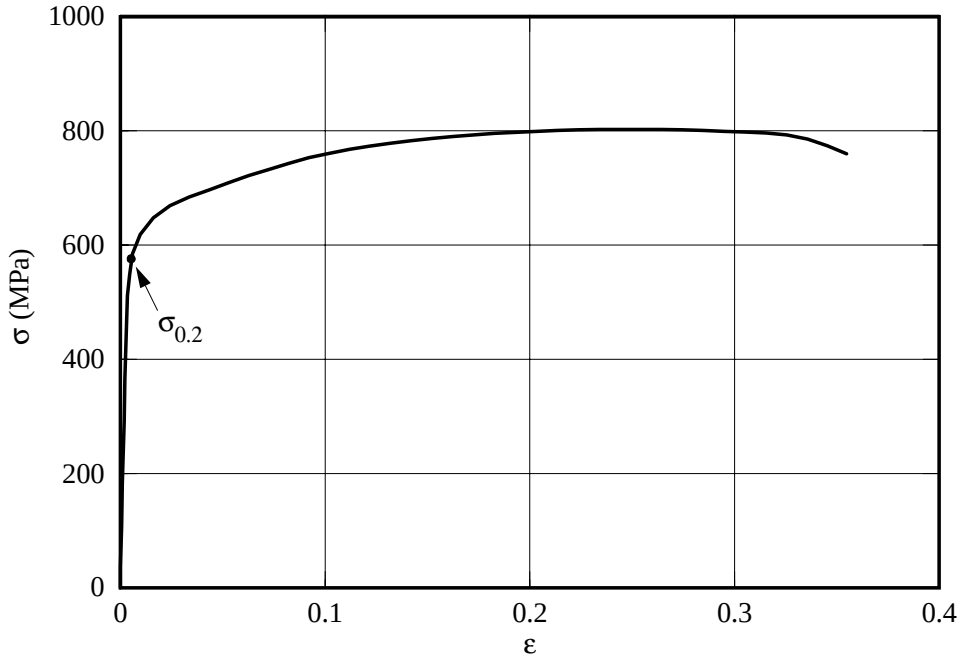

Figure A1: Stress strain curves for longitudinal tension (LT)

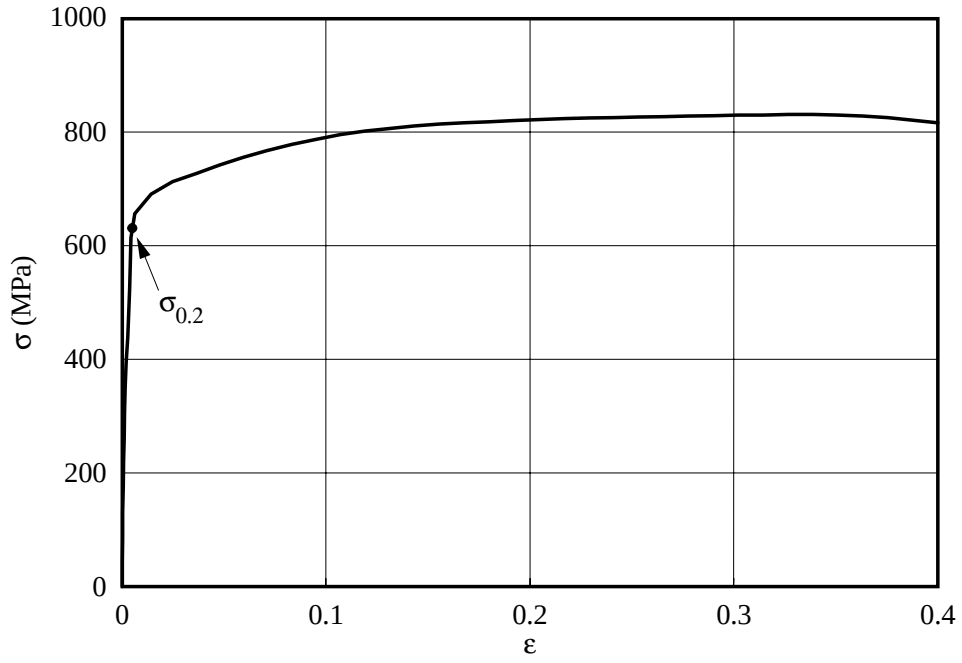

Figure A2: Stress strain curves for transverse tension (TT)

Appendix B: Comparison of strains for test plate SS250, test and Abaqus models Iso_pp_1hw and Aniso_pp_1hw

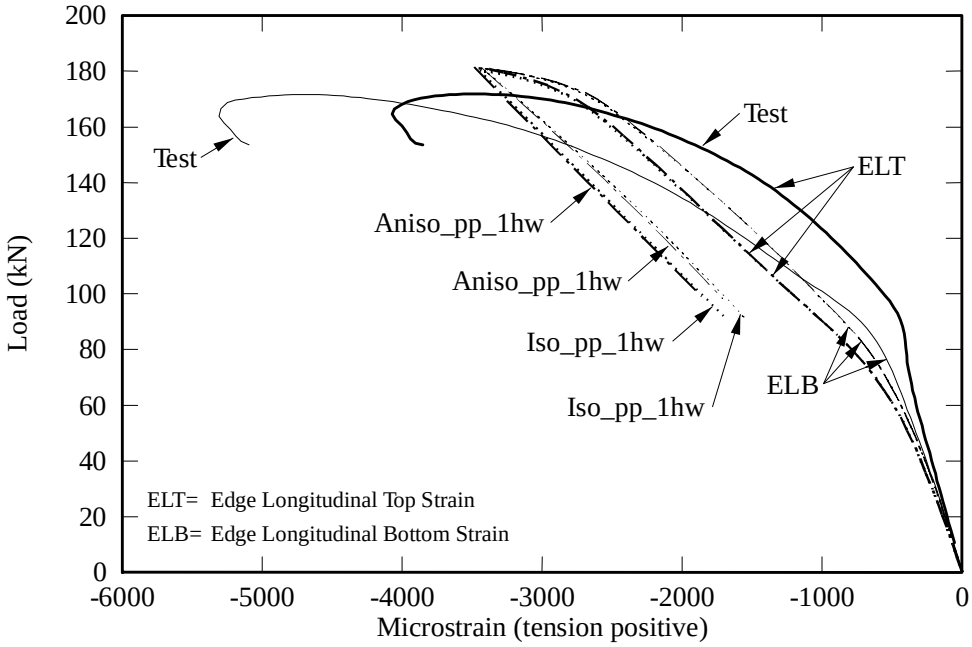

Figure B1: Longitudinal Strains 15 mm from Edge for Test Plate SS250; Test and Abaqus Models Iso-pp-1hw and Iso-pp-1hw

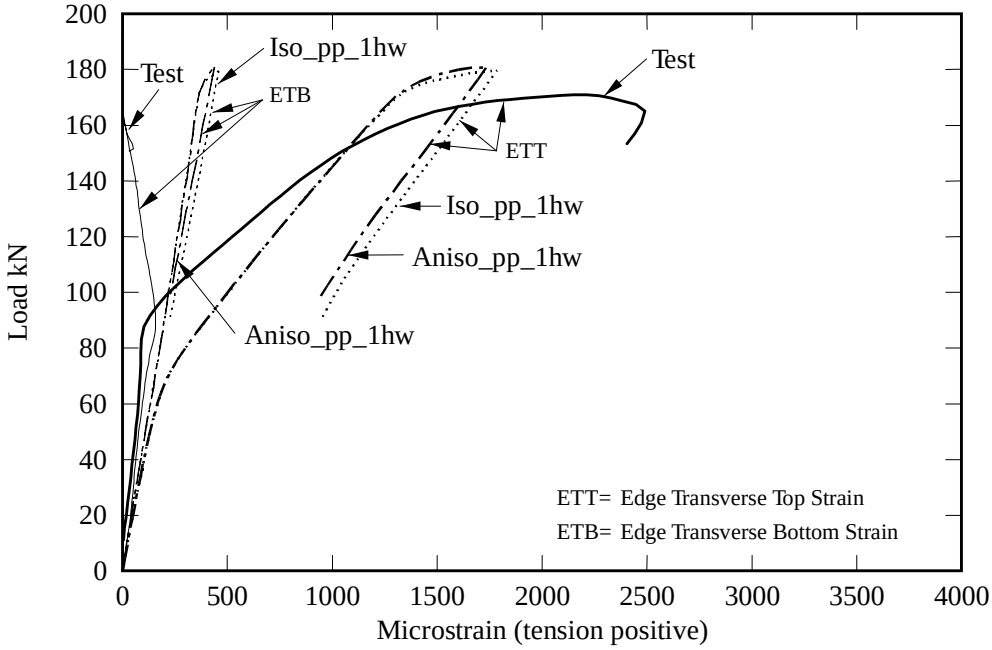

Figure B2: Transverse Strains 15 mm from Edge for Test Plate SS250; Test and Abaqus Models Iso-pp-1hw and Iso-pp-1hw

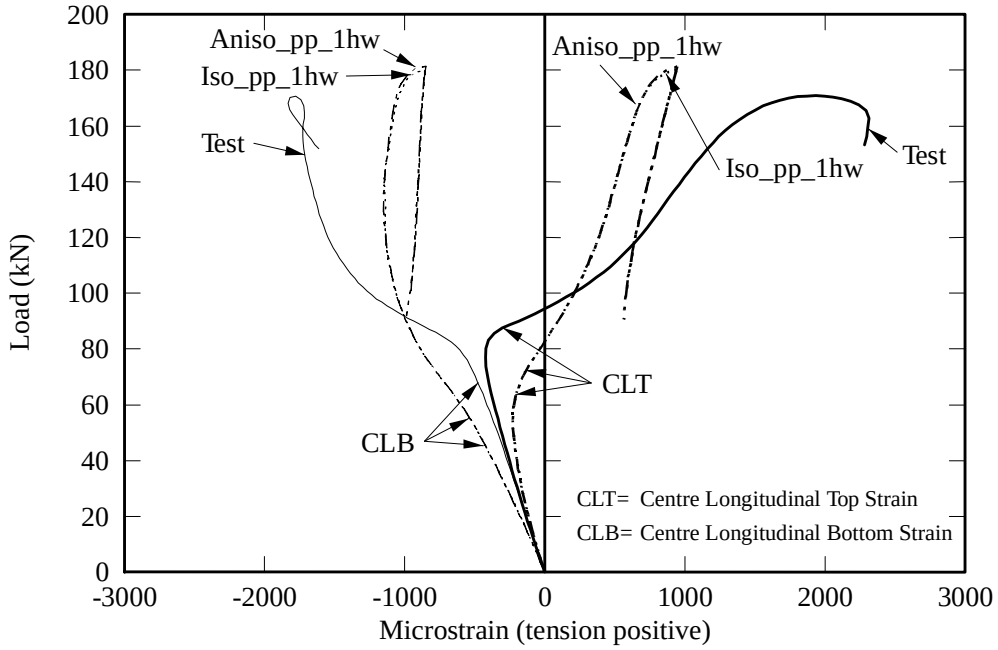

Figure B3: Longitudinal Strains at centre for Test Plate SS250; Test and Abaqus Models Iso-pp-1hw and Aniso-pp-1hw

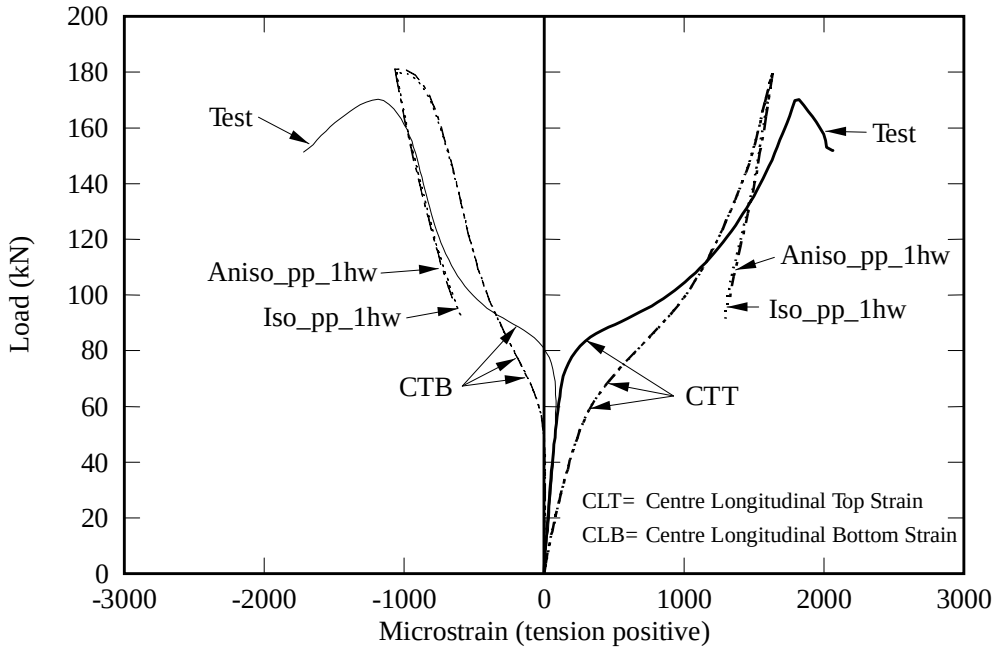

Figure B4: Transverse Strains at centre for Test Plate SS250; Test and Abaqus Models Iso-pp-1hw and Aniso-sh-1hw